Molecular charge transport : relating orbital structures to the conductance properties

Guédon, C.M.

Citation

Guédon, C. M. (2012, November 6). *Molecular charge transport : relating orbital structures to the conductance properties*. *Casimir PhD Series*. Retrieved from https://hdl.handle.net/1887/20093

Author: Guédon, Constant Marcel
Title: Molecular charge transport : relating orbital structures to the conductance properties
Issue Date: 2012-11-06

C

Complementary information on chapter 6

C.1 Formation and analysis of the Self-Assembled Monolayers

Self-Assembled Monolayers (SAMs) of the acetyl-protected mono- and dithiols were grown from solutions with triethylamine as deprotecting agent, which promotes the formation of high-quality and densely-packed SAMs, as recently showed for acetyl-protected OPE dithiols and monothiols[1]. Due to the low solubility of the AC- and AQ-compounds in THF, these SAMs were grown from 0.5 mM solutions in chloroform (Aldrich, anhydrous, =99%, stabilized by amylenes) with 10% (v/v) triethylamine (Fisher, HPLC grade, degassed) added. The SAMs of the OPE mono- and dithiol were grown from 0.5 mM solutions in dry THF, with 10% (v/v) triethylamine added. All solutions and SAMs were prepared inside a glovebox filled with nitrogen (<5 ppm O_2). We used freshly prepared samples of 150 nm gold on mica for the ellipsometry and XPS studies, and freshly prepared samples of 5 nm chromium and 200 nm gold thermally deposited on a silicon wafer for the CP-AFM studies. Samples were immersed upside down for two nights in about 3 mL solution. After this immersion time, the samples were taken from solution, rinsed three times with clean THF, and dried on the nitrogen atmosphere in the glovebox.

Ellipsometry measurements were performed using a V-Vase from J. A. Woollam Co., Inc. in air. Measurements were acquired from 300-800 nm with an interval of 10 nm at 65, 70, and 75 ° angle of incidence. For every set of experiments a fresh gold-on-mica sample was measured at three or four different spots. The data from these measurements were merged and the optical constants were fitted. For every SAM three spots were measured and the thickness of a cauchy layer (n=1.55, k=0 at all λ) on top of the gold layer was fitted and averaged over the three spots.

X-ray Photoelectron Spectroscopy (XPS) measurements were performed on a X-PROBE Surface Science Laboratories photoelectron spectrometer with a Al Ka X-ray source (1486.6 eV) and a takeoff angle of 37ž. We accumulated 20 scans for S2p, 10 for C1s, 10 for O1s, 15 for N1s, and 5 for Au4f. All reported data are averaged over four different spots per sample and presented in table C.1. WinSpec[1] was used to fit the recorded data with a background and minimum number of mixed Gaussian-Lorentzian singlets (C1s, N1s, O1s) or doublets (Au4f; Δ=3.67 eV, S2p; Δ=1.18 eV) with a width of 1.21 eV.

Molecular wire	**Au4f** (84 eV)	**C1s** CxHx (283 -287 eV)	**C1s** C=O (288 eV)	**S2p** S-Au (162 eV)	**S2p** S-R (164 eV)	**O1s** (532 eV)	Normalized intensities **C1s** per C-atom
AC-DT	7515	1343	39	19	84	57	43
AQ-DT	7564	1017	73	18	55	102	36

TABLE C.1: Composition of the SAM's: X-ray photoelectron spectroscopy measurements. The integrated intensities are divided by the sensitivity factor: 1 for C1s, 1,79 for S2p and 2,49 for O1s

We determined the thicknesses of the SAMs from our XPS results by two different methods: A) from the ratio between the carbon and the gold signals[2] and B) from the attenuation of the gold signals[3].
Method A. Thicknesses of the SAMs(d_{CS}) are determined from the ratio of the areas of C1s and Au4f peaks by equation C.1 with λ_{Au} = 31 Å, λ_C = 27 Å, $d_C = d_{CS} - 1.8$ Å(d_C is the thickness of the hydrocarbon layer without the thiolate); k is estimated to be 0.15 from XPS measurements on a SAM of undecanethiol

---

[1] WinSpec 2.09, developed at Laboratoire Interdépartemental de Spectroscopie Electronique, Namur, Belgium

on gold. We determined d$_{CS}$ from I_C/I_{Au} by an iterative numerical approach.

$$\frac{I_c}{I_{Au}} = k\frac{1-\exp(\frac{-d_c}{\lambda_C})}{\exp(\frac{-d_{CS}}{\lambda_{Au}})} \tag{C.1}$$

Method B. Thicknesses (d) are determined from the attenuation of the Au4f signal by equation C.2 with Au0 = 109754, λ = 42 Å, and θ = 37ř.

$$I_{Au} = I_{Au0}\exp(\frac{-d}{\lambda sin\theta}) \tag{C.2}$$

We found a good agreement between the length of the molecules and the thickness of the SAMs, indicating the formation of densely-packed monolayers in which the molecules are oriented nearly perpendicular to the gold substrate surface.

Molecular wire	Length^a (Å)	Ellipsometry (Å)	XPS method A (Å)	XPS method B (Å)	Weighed Average^b (Å)
AC-DT	24.49	28.6*	24.1	27.1	25
AQ-DT	24.49	21.7	20.1**	26.9	24
OPE-DT	20.14	19.7	17.5	17.8	19

TABLE C.2: a: The distance from S- to S-atom as obtained by DFT calculations.
b: The thicknesses as obtained by ellipsometry and XPS are averaged. The absolute values obtained from XPS by method A are considered more accurate than those obtained by method B and therefore weighed twice as strong. Identical weights were used for ellipsometry and XPS (methods A and B combined).
*: The value for **AC-DT** as determined by ellipsometry is not included in the average, since this large (highly reproducible) value is likely to be caused by the optical absorption of this compound in the range of the ellipsometry measurement.
: The value for **AQ-DT as determined by XPS method A is not included in the average, because the oxygen atoms from the anthraquinone core do attenuate the Au signal, but do not contribute to the carbon signal, underestimating the actual thickness.

The SAMs of the monothiolated molecular wires were measured by ellipsometry. The thickness of the SAMs was 17.5 Åfor **AQ-MT** and 20.5 Åfor **OPE-DT**.

From the XPS data, the ellipsometry measurements and DFT calculations we find a densely packed, upright standing SAM for AQ-DT and AC-DT.

C.2 DATA ANALYSIS

The current-voltage data gathered for each sample are put together and analyzed further using a MatLab code. For the figures in the main text, around 95

% of the measured curves are used. A small number of curves have been removed. The curves showing no contact with molecules i.e. below the noise level of our set-up (typically ≈ 100 pA) are removed from our data set. In fact this is the case when no contact is formed with the SAM. Additionally we removed the curves presenting saturation, indicating direct contact between the tip and the gold bottom electrode. In figureC.1 we show typical single I(V) curves of data kept and removed. table II summarizes the amount of removed data, which is typically as little as 5 % of the data.

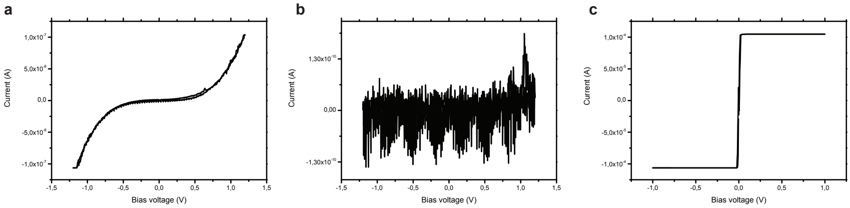

FIGURE C.1: **a**, typical I(V) curve kept in our data set for **AQ-MT**, **b**, typical I(V) curve below detection limit of our set-up, **c**, typical I(V) curve showing saturation of the current amplifier for **AQ-MT**.

Molecule	number of curves	number of curves rejected	% rejected
AC-DT	1979	98	4.9 %
AQ-DT	2502	107	4.3%
AQ-MT	2884	251	8.7%
OPE3-DT	621	32	5.1%
OPE3-MT	1574	65	4.1%

TABLE C.3: table showing the amount of curves disregarded due to no contact or saturation for the different molecules measured

Second the remaining I(V) curves are smoothed with a local regression using weighted linear least squares and a 2nd degree polynomial model. Next we take a numerical derivative of the current relative to the voltage (dI/dV). Finally we construct a 2D histogram of these dI/dV values by logarithmically binning them for each bias voltage and plotting them next to each other. This will result in a 3D graph with on the x-axis the bias voltage, on the y-axis the log (dI/dV) and on the z-axis (in colour scale) the number of counts. Such a 2D histogram can be seen as a collection of traditional 1D conductance histograms for different bias voltages. In figureC.2 we show such 2D histogram for **AQ-MT** for both the full data set (figureC.2a) and the partial data set (figureC.2b). It is clear from this comparison that removing the contacted and saturated curves makes the picture more clear. However in the full data set plot the trend in the dI/dV curve is still easily distinguishable. We also refer to the section Supplementary Figures, where we display raw I(V)-curves, both as an ensemble and individually, and present alternative methods of analyzing the data.

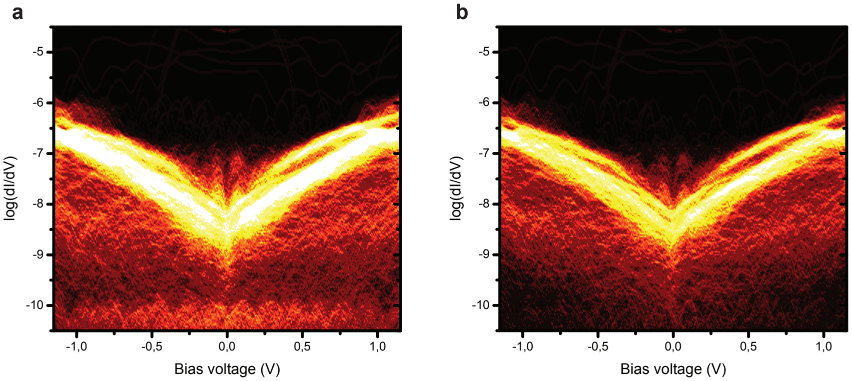

FIGURE C.2: dI/dV (Ω^{-1}) 2D histogram for **AQ-DT** **a**, without data rejected and **b**, with data rejected i.e. the curves with no contact and the saturated curves

C.3 CALCULATIONS

Below we present our conductance calculations in more detail. Furthermore, we elaborate on the relationship between the transmission function $T(E)$ and dI/dV-curves.

C.4 TRANSMISSION CALCULATIONS

The conductance is calculated using DFT in combination with a non-equilibrium Green function (NEGF) method as described in Ref. [4]. Our DFT-NEGF method is implemented in GPAW, which is a real space electronic structure code based on the projector augmented wave method [5, 6]. We use the Perdew-Burke-Ernzerhof (PBE) exchange-correlation functional [7], and a 4×4 k-point sampling in the surface plane. The electronic wave functions are expanded in an atomic orbital basis [6]. All atoms are described by a double-zeta plus polarization (dzp) basis set. We initially relax the molecule and the two closest Au layers until the forces on the atoms are less than 0.05 eV/Å. In the relaxed configuration, the S-atoms bind to Au at a bridge site slightly shifted toward the hollow site.

Following the standard DFT-Landauer approach, we calculate the zero-bias transmission function,

$$T(E) = \mathrm{Tr}[\mathbf{G}^r(E)\Gamma_L(E)\mathbf{G}^a(E)\Gamma_R(E)], \tag{C.3}$$

with $\mathbf{G}^r(E) = (E\mathbf{S} - \mathbf{H} - \Sigma_L(E) - \Sigma_R(E))^{-1}$ being the retarded Green's function for the junction (scattering region) described by the single-particle Hamiltonian $\mathbf{H}$ and overlap matrix $\mathbf{S}$, and where the semi-infinite electrodes are included through left and right self-energies, $\Sigma_{L,R}(E)$. The advanced Green's function $\mathbf{G}^a(E) = (\mathbf{G}^r(E))^\dagger$, and $\Gamma_{L,R}(E) = i(\Sigma_{L,R}(E) - \Sigma_{L,R}(E)^\dagger)$. The low-bias conductance can finally be obtained from the Landauer formula, $G = (2e^2/h)T(E_F)$, where E_F is the Fermi energy.

The DFT transmission for **AC-DT**, **AQ-DT**, and **AQ-MT** is shown in figureC.3.

C.5 CORRECTION OF HOMO-LUMO GAP

It is well known that DFT is unable to accurately describe energy gaps and level alignment of molecules at surfaces [8]. To correct for this inability we use a self-energy correction scheme (DFT+Σ) that has recently been shown to predict conductance values in good agreement with single-molecule experiments [9, 10]. In the DFT+Σ approach we initially correct the gas phase HOMO-LUMO gap.

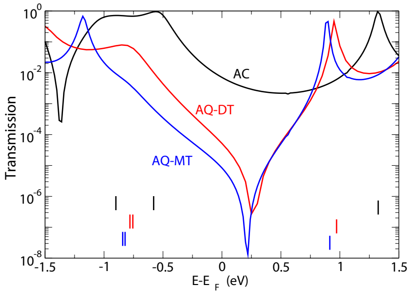

FIGURE C.3: Transmission function vs. energy calculated with with standard DFT + NEGF methods. The vertical bars mark the HOMO and HOMO-1 (to the left) and LUMO (to the right) positions. The qualitative shapes of the transmission functions are the same as for the DFT+Σ results shown in the main text, Fig. 2 (a)

This is done by calculating the ionization potential (IP) and electron affinity (EA) from total energy calculation:

$$\begin{aligned} \text{IP} &= E(+e) - E(0) \qquad \text{(C.4)} \\ \text{EA} &= E(0) - E(-e), \qquad \text{(C.5)} \end{aligned}$$

where $E(0)$ is the total energy of the neutral molecule, $E(+e)$ is the energy of the molecule with one electron removed (i.e. positively charged), and $E(-e)$ is the total energy of the molecule with one extra electron on it. The gas phase HOMO-LUMO gap is calculated as ΔE =IP-EA. The calculated values are shown in tableC.4. ε_{LUMO}, corresponding to the highest occupied and lowest unoccupied eigenstates. As shown in tableC.4, the corresponding HOMO-LUMO gaps, $\Delta\varepsilon$, are significantly lower than the ones calculated from total energies, and the self-energy correction should thus shift the occupied states down in energy and the unoccupied states up in energy thereby opening the gap. When a molecule is brought close to a metallic surface, image charge interactions will further change the energy levels resulting in a shift of the occupied levels *up* in energy and the unoccupied states *down* in energy. From a simple electrostatic model [9] we get that the electrostatic interactions closes the HOMO-LUMO gap of **AC-DT** and **AQ-DT** by $\Delta_q = 1\,\text{eV}$ in total: 0.5 eV upward shift of the occupied and -0.5 eV downward shift of the unoccupied states. The electrostatic interaction is slightly larger for the OPEs because they are shorter, and we get a gap closing of $\Delta_q = 1.2\,\text{eV}$ in total. The resulting shifts of occupied states is then

$$\Sigma_{occ} = -IP - \varepsilon_H + \Delta_q/2 \qquad \text{(C.6)}$$

	IP	EA	ΔE	ε_H	ε_L	$\Delta\varepsilon$	Σ_{occ}	Σ_{unocc}	$T_0(E_F)$	$T_\Sigma(E_F)$
AC	6.20	1.59	4.61	-4.87	-3.08	1.79	-0.83	0.99	$7.1\cdot 10^{-3}$	$0.5\cdot 10^{-3}$
AQ-DT	6.44	2.21	4.23	-5.42	-3.84	1.58	-0.52	1.13	$4.6\cdot 10^{-5}$	$1.1\cdot 10^{-5}$
AQ-MT	6.73	2.21	4.52	-5.46	-3.87	1.59	-0.77	1.16	$8.3\cdot 10^{-6}$	$5.7\cdot 10^{-7}$
OPE-DT	6.45	1.22	5.23	-4.99	-2.78	2.21	-0.86	0.96	$1.6\cdot 10^{-2}$	$1.7\cdot 10^{-3}$
OPE-MT	6.64	1.19	5.46	-5.08	-2.79	2.29	-0.96	1.01	$6.2\cdot 10^{-4}$	$5.5\cdot 10^{-5}$

TABLE C.4: Ionization potential (IP), electron affinity (EA), and corresponding HOMO-LUMO gap, ΔE, obtained from total energy calculations. Kohn-Sham HOMO, ε_H, LUMO, ε_L energy and corresponding gap, $\Delta\varepsilon$. In the DFT+Σ method, the occupied (unoccupied) states are shifted by Σ_{occc} (Σ_{unocc}). $T_0(E_F)$ is the pure DFT transmission values at the Fermi energy and $T_\Sigma(E_F)$ is the value obtained with the DFT+Σ approach. All energies are given in units of eV.

and of the unoccupied states

$$\Sigma_{unocc} = EA + \varepsilon_L - \Delta_q/2. \tag{C.7}$$

The calculated values are shown in tableC.4. When comparing the DFT+Σ transmissions in the main text, Fig. 2(a) with the pure DFT results in figureC.3 we see that the effect of Σ merely is to shift the occupied states down in energy and the unoccupied states up in energy. While the qualitative behaviour and the shape of the transmission functions are relatively unchanged the overall magnitude and quantitative details are changed. Previous studies [9, 10] have shown that DFT+Σ yields better agreement with experiments.

figureC.4 shows the OPE transmissions calculated with the DFT+Σ method.

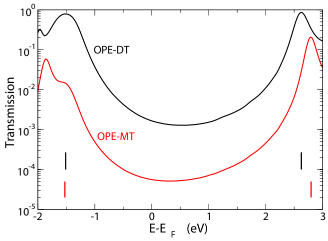

FIGURE C.4: Transmission function calculated with DFT+Σ for **OPE-DT** and **OPE-MT**.

C.6 DI/DV CURVES

We calculate current-voltage relations from the low-bias transmission function. As discussed in the main text, we allow for an energy shift ΔE of the Fermi level. We also allow for an asymmetric voltage drop at the left and right electrodes described by the parameter η. Based on previous finite bias DFT calculations[11] on similar molecules, we use an estimated value of $\eta = 0.6$ for all the mono-thiols. The main conclusions are, however, independent of this specific choice. For the di-thiols we assume a symmetric voltage drop with $\eta = 1/2$.

The current is calculated as

$$I(V) = \frac{2e}{h}\int_{-\infty}^{\infty} T(E+\Delta E)\left\{f_L[V\eta] - f_R[V(\eta-1)]\right\} \mathrm{d}E, \tag{C.8}$$

where $f_{L/R}(V) = 1/[\exp(E_F + eV)/k_B T + 1]$ are the Fermi-Dirac distributions for the left and right contact. The dI/dV curves are found by differentiation of (C.8). Results for AQ-MT and OPE-MT are shown in the main text (Fig. 4), while dI/dV curves for AQ-DT, AC-DT, and OPE-DT are shown in figureC.5, for various values of ΔE.

The most important case is that of AQ-DT (left panel). Let us extend the discussion at the end of the main paper while inspecting figure C.5. Just like for AQ-MT (see Fig. 4a), we see that for AQ-DT, the shape of the dI/dV curves depends strongly on the energy shift ΔE. For $\Delta E = -0.7$ eV, the calculations of dI/dV yield a clear zero-bias anomaly for AQ-DT. The reason is that in that case, the dip in the transmission function $T(E)$ lies very close to the Fermi level (in the section below, we go into this more generally). However, for other values of ΔE, the shape of the dI/dV curves tends towards a parabola-like curve. The latter is in correspondence with our measurements in Fig. 3a, where we find a strongly suppressed conductance for AQ-DT (with respect to AC-DT), but no zero-bias anomaly. In other words, although both AQ-DT and AQ-MT exhibit quantum interference, the zero-bias anomaly is only visible for AQ-MT, since for that molecule the transmission dip is much closer to E_F.

Of course, we need to consider the question why the transmission minimum is shifted to different positions for AQ-DT and AQ-MT. This is explained by the fact that AQ-DT junctions comprise two Au-S dipoles, whereas AQ-MT junctions have only one. The accompanying charge transfer results in a higher upward energy shift for the transmission function of AQ-DT than for AQ-MT (by ≈ 0.2 eV in our calculations). Hence, in AQ-DT, the transmission dip is positioned more above E_F. Consequently, no anomaly shows up in dI/dV-curves as illustrated in figure C.5. Interestingly, the inherent difference in charge transfer for AQ-DT and AQ-MT implies that it is very unlikely to see a zero-bias anomaly in the dI/dV-curves of both AQ-DT and AQ-MT.

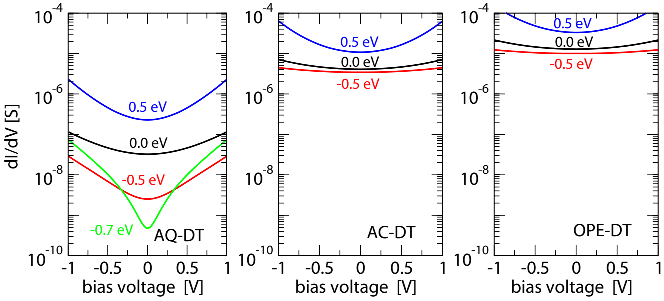

FIGURE C.5: dI/dV -curves calculated from the transmission function shifted by $\Delta E = 0.0$ eV $\Delta E = 0.5$ eV and $\Delta E = -0.5$ eV, relative to the Fermi energy. In the case of AQ-DT (left panel), we also show the result for $\Delta E = -0.7$ eV to illustrate that a dI/dV dip similar to that experimentally seen for AQ-MT could in principle be observed for AQ-DT, with a larger energy shift. In order to simulate the experimental situation with multiple molecules in contact with the AFM tip, the DFT+Σ transmission functions have been multiplied by a factor of 100.

C.7 RELATIONSHIP BETWEEN DI/DV CURVES AND THE POSITION OF THE MINIMUM IN T(E)

In the previous section, we stated that an anti-resonance in $T(E)$ leads to an anomaly in dI/dV only if this anti-resonance is situated near the Fermi level. Here, we discuss this relationship further, first mathematically, then with a model calculation.

Mathematically, the relation between dI/dV and $T(E)$ can be written (using the Landauer formula at $T = 0$K) as:

$$\frac{\mathrm{d}I}{\mathrm{d}V} = \frac{2e^2}{h}(\eta T(E_F + \eta eV) + (1-\eta)(T(E_F - (1-\eta)eV))) \tag{C.9}$$

where η expresses the symmetry of the junction ($\eta = 0.5$ for a symmetric junction). As a first consequence, symmetric dI/dV-curves are necessarily obtained for symmetrically coupled molecules, irrespective of the (a)symmetry of T(E) around the Fermi level E_F. This is easily seen by inserting $\eta = 0.5$ into the formula above, and interchanging +V and -V.

Indeed, from eq. C.9, we can also see that if the dip in $T(E)$ is located at or near E_F, the dI/dV-curves will show a zero-bias anomaly. However, if the anti-resonance of $T(E)$ does not lie close to E_F, no dip will be observed in dI/dV. To understand this, let us suppose the transmission dip is significantly above E_F, at a distance δE. Then, it will come inside the bias window at a bias voltage

$eV = \delta E/\eta$. At this voltage, the first term in the expression will obviously become very small. However, there is still the second term (the negative border of the bias window), which will not be small at all (cf. Fig. 2a and note the logarithmic scale). Hence, the second term will dominate the conductance and the dip is washed out. We note that this reasoning also holds if the dip in $T(E)$ is below E_F, provided the molecular junctions are nearly-symmetrically coupled. Only if the asymmetry is very strong ($\eta = 0$ or $\eta = 1$), one could probe a dip at non-zero biases. However, this limit is only attained under strong tunnelling conditions and it is not relevant for the junctions considered here. For our experiments, we have η between symmetric (0.5, for dithiols) and moderately asymmetric (0.6, monothiols).

To further illustrate this, we make use of a model tight binding calculation of $T(E)$. In figureC.6 (left panel), we show three transmission functions, that differ only by a shift in energy. Three cases are chosen: one in which the minimum of $T(E)$ is exactly at E_F (red), one where it is 0.4 eV below E_F (black), and one where it is 0.2 eV above E_F. The peaks where $T(E) = 1$ correspond to the position of the HOMO and LUMO resonances. The resulting $\mathrm{d}I/\mathrm{d}V$-curves are shown in the right panel of figureC.6 (same colour coding). These $\mathrm{d}I/\mathrm{d}V$-curves have been calculated from formula (C.8) using asymmetry parameters of $\eta = 0.5$ (full line) and $\eta = 0.6$ (dashed line). These values correspond to voltage drop occurring symmetrically and slight asymmetrically over the molecule, respectively. The symmetric choice applies to our dithiol bonded jucnctions while the slightly asymmetric corresponds to our monothiol bonded junctions. The value $\eta = 0.6$ is estimated on basis of first-principles finite bias calculations for similar molecular junctions [11].

It is clear from figureC.6 that the characteristic V-shape in the dI/dV, observed for AQ-MT in Fig. 3 of the main paper, only appears when the transmission node is positioned close to the Fermi energy. When the transmission node appears below or above the Fermi energy, the shape of the dI/dV is parabola-like, similar to that observed for the conjugated molecules OPE3 and AC, see Figs. 3c-d and Fig. 1c. This shows that the presence of QI is a necessary but not a sufficient condition for observing a dip in the dI/dV curve. In particular it shows that in cases where the transmission dip lies away from the Fermi energy, destructive QI would reveal itself as a strong reduction of the numerical value of the conductance rather than a qualitative effect on the $\mathrm{d}I/\mathrm{d}V$-curve. This is indeed what we observe experimentally for AQ-DT.

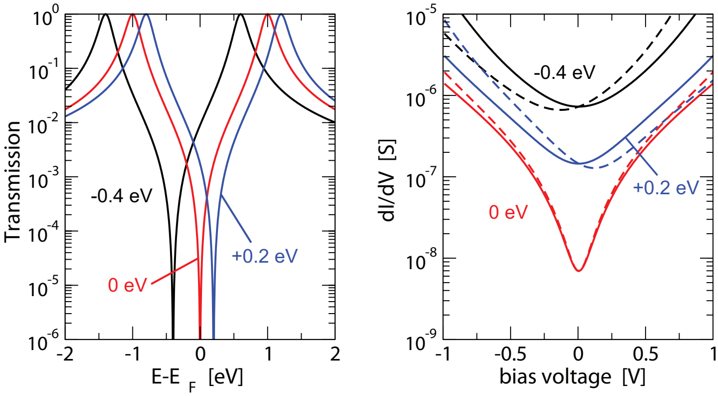

FIGURE C.6: Left panel: Calculated transmission function for a model tight binding calculation. The three curves shown are similar, but the transmission minimum is shifted in energy with respect to E_F, i.e., by −0.4 eV (black), 0 eV (red) and +0.2 eV (blue), respectively. The right panel shows the corresponding dI/dV curves (same colour coding). They have been obtained from equation C.8 assuming a symmetric junction with $\eta = 0.5$ (full line) and slightly asymmetric junction with $\eta = 0.6$ (dashed line), respectively.

C.8 3-SITE MODEL

We shall now show that the two different paths in the three site model have a phase difference of π, and thus contribute with different signs. The three-site model derived from localized molecular orbitals (LMOs) is shown in figure C.7 with the LMO on-site energies and hopping parameters indicated.

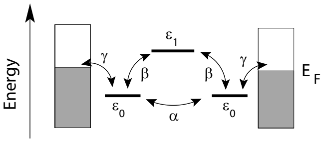

FIGURE C.7: Three-site model with on-site energies and hopping parameters indicated. For the calculations in Fig. 2 in the main text we use $\varepsilon_0 = -1.2\,\text{eV}$, $\varepsilon_1 = 2.1\,\text{eV}$, $\alpha = 0.04\,\text{eV}$, $\beta = 0.24\,\text{eV}$, and $\gamma = 0.4\,\text{eV}$.[12]

Since only the left and right orbitals couple to the left and right electrodes, respectively, the coupling matrices $\Gamma_{L,R}$ in Eq. (C.3) have the shapes

$$\Gamma_L = \begin{pmatrix} \gamma & 0 & 0 \\ 0 & 0 & 0 \\ 0 & 0 & 0 \end{pmatrix}, \quad \Gamma_R = \begin{pmatrix} 0 & 0 & 0 \\ 0 & \gamma & 0 \\ 0 & 0 & 0 \end{pmatrix}, \tag{C.10}$$

where we have assumed that the coupling is energy independent (the wide band limit approximation). From the general transmission formula (C.3) we then get

$$T(E) = \gamma^2 |\mathbf{G}_{12}(E)|^2, \tag{C.11}$$

so the transmission is determined by the (1,2) matrix element of the Green's function. Physically this quantity describes the propagation of an electron from site '1' (left) to site '2' (right). The 3-site Hamiltonian may be written as $\mathbf{H} = \mathbf{H_0} + \mathbf{V}$, where

$$\mathbf{H}_0 = \begin{pmatrix} \varepsilon_0 & 0 & 0 \\ 0 & \varepsilon_0 & 0 \\ 0 & 0 & \varepsilon_1 \end{pmatrix} \tag{C.12}$$

is the on-site Hamiltonian and

$$\mathbf{V} = \begin{pmatrix} 0 & \alpha & \beta \\ \alpha & 0 & \beta \\ \beta & \beta & 0 \end{pmatrix} \tag{C.13}$$

is the coupling between the sites. We now consider the two routes separately and set $\alpha = 0$ for the upper route and $\beta = 0$ for the lower route. Treating $\mathbf{V}$ as a perturbation we may obtain the full Green's function from the Dyson equation

$$\mathbf{G} = \mathbf{G}_0 + \mathbf{G}_0 \mathbf{V} \mathbf{G}, \tag{C.14}$$

where $\mathbf{G}_0(E) = (E\mathbf{I} - H_0 - \Sigma_L - \Sigma_R)^{-1}$, and the self energy matrices are related to the Γ-matrices by $\Gamma_{L,R}(E) = i(\Sigma_{L,R}(E) - \Sigma_{L,R}(E)^\dagger)$. For the lower route we iterate the Dyson equation (C.14) once to get the lowest order contribution and find

$$G_{1,2}^{lower} = \frac{\alpha}{(E - \varepsilon_0 + i\gamma/2)^2}. \tag{C.15}$$

Taking the upper route we need to iterate the Dyson equation twice (since there are two hops from left to right) and get

$$G_{1,2}^{upper} = \frac{\beta^2}{(E - \varepsilon_0 + i\gamma/2)^2 (E - \varepsilon_1)}. \tag{C.16}$$

Taking the ratio of the two contributions

$$\frac{G_{1,2}^{upper}}{G_{1,2}^{lower}} = \frac{\beta^2(E-\varepsilon_1)}{\alpha}, \tag{C.17}$$

we observe that for energies $E < \varepsilon_1$ the ratio has a *negative sign* showing that the two paths have a phase difference of π. Since the transmission depends quadratically on the Green's function element, the transmission through the three-site model is to leading order given by

$$T(E) = |\sqrt{T_{upper}} - \sqrt{T_{lower}}|^2. \tag{C.18}$$

for energies $E < \varepsilon_1 \approx E_{LUMO}$.

C.9 MEASUREMENTS ON OTHER SAMPLES

Here we present supplementary figures showing results for **AQ-MT** for different samples (named sample 2 and 3 for clarity). First the 2D histogram of **AQ-MT** for sample 2 is shown in figureC.8. The overall shape of the dI/dV curves shown in figure 3b is well reproduced on this sample although the conductance values are lower than the ones found in figure 3b in the main text. The number of contacted molecules varies from tip to tip due to intrinsic differences in tip geometry. The displayed dI/dV curve is in agreement with theoretical calculations (see figure 4a, with a -0.5 eV shift) assuming we have 100 molecules bridging the junction.

A similar V-shaped dI/dV -curve is observed in the data displayed in figureC.9a. However, here the conductance values are much larger than in figure 3b of the main text. To investigate this interesting case further, we took a closer look at the tip geometry. On the scanning electron micrographs shown in figureC.9b we can clearly see the remains of a broken cantilever next to and more importantly below the actual cantilever used.

As a result the contact area in this case is much larger than for a regular tip i.e. much more molecules are contacted. Hence, this experimental incident confirms that the conductance is dependent on the number of molecules contacted. However, such an increase in contacted molecules does not affect the typical shape of the dI/dV-curve. We therefore show here that the overall shape of the dI/dV is independent on the number of molecules contacted.

C.10 I(V)-CURVES AND ALTERNATIVE ANALYSIS

Here, we inspect the raw I(V)-curves obtained for AC-DT, AQ-DT and AQ-MT in more detail. We do so both for individual curves and for the ensemble of I(V)'s.

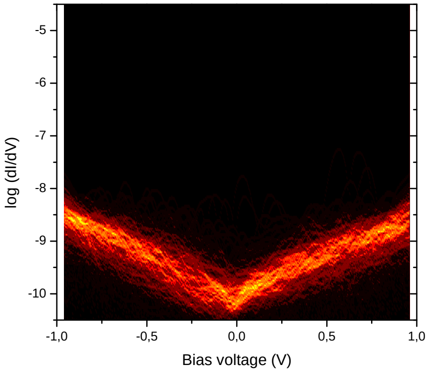

FIGURE C.8: 2D histogram for **AQ-MT** on sample 2 with the dI/dV (Ω^{-1})

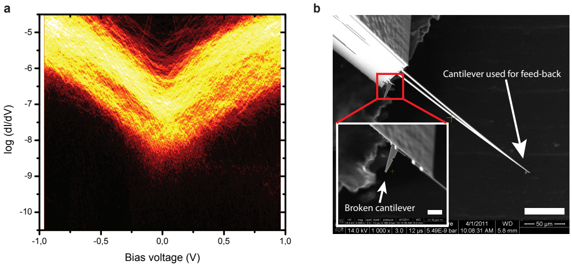

FIGURE C.9: **a**, 2D histogram for **AQ-MT** on sample 3 with the dI/dV (Ω^{-1}). **b**, SEM picture of the tip used for measurements shown in panel **a**. The overview of the chip is shown with the cantilever used and the remains of the broken one clearly at a lower position. In the inset we show a magnified picture of the broken cantilever. The scale bar in the picture is 50 μm and 10 μm in the inset.

This allows us to demonstrate the robustness of the features displayed in Figs. 1c (AC-DT) and 3a (AQ-DT) and 3b (AQ-MT).

In the Supplementary Methods section, we have explained how individual I(V)-curves are treated to obtain a 2D-histogram of dI/dV data for the ensemble. For AQ-MT, a clear zero-bias anomaly is observed in the resulting 2D-histogram (Fig. 3b). Here, we go back to the individual measurements to check that the zero-bias anomaly is truly intrinsic to single I(V)-curves. In figure C.10, we show three representative I(V)-curves for AQ-MT (a subset of the data in Fig. 3b, another curve is shown in figure C.1a). Each contains 1000 points, taken at a sample rate of 10 kHz (i.e. 0.1 s per curve). Raw data are presented, with original noise and a slight hysteresis. The latter is a result of the relatively large RC-time of the system at these high resistances. In figure C.11, we show a representative I(V)-curve for AC-DT. Upon inspection by eye, there is indeed a difference between the I(V)'s for AQ-MT and AC-DT. Whereas the curves in figure C.10 display a plateau with near-zero slope around zero bias, the curve in Fig. SC.11 has finite slope around zero bias. However, this distinction may be in the eye of the beholder. For that reason, we have taken the derivative of the individual I(V)'s, after smoothing. The resulting dI/dV-curves are displayed in Figs. SC.10b, d, and f for the AQ-MT case. Clearly, these curves show a negative curvature, except near zero bias where an anomaly is seen. This demonstrates that the anomaly in Fig. 3b stems from the individual I(V)-curves indeed. figureC.11b shows the dI/dV calculated from figure C.11a. It shows the same parabola-like shape that we found in Fig. 1c.

Now that we have checked individual I(V)- and dI/dV-curves, let us turn to the full ensembles of I(V)-curves. In figure C.12, we present the full batch of I(V)-curves for AC-DT (corresponding to Fig. 1c), AQ-DT (cf. Fig. 3a) and AQ-MT (samples presented in Fig. 3b and in figure C.9, i.e. with broken tip), respectively. To allow for a good comparison between the data sets for different molecules, all I(V)-curves have first been normalized in the current scale. Apart from that, these are raw data. Upon visual inspection, a plateau around zero bias is visible for the AQ-MT data set (Fig. SC.12c,d), which is not there for AC-DT and AQ-DT. However, such a distinction should be checked to be independent of the observer. It is for that reason that we performed the data analysis described in the Supplementary Methods section. Clearly, it is also important to demonstrate that the final conclusions do not depend on the exact analysis method chosen. Hence, we use a different statistical treatment below, by first determining average I(V)'s for the entire batch and then calculating the corresponding dI/dV.

In all panels of figure C.12, a red line represents the average of all I(V)-curves in the panel. In addition, a blue line represents an average of all curves, after

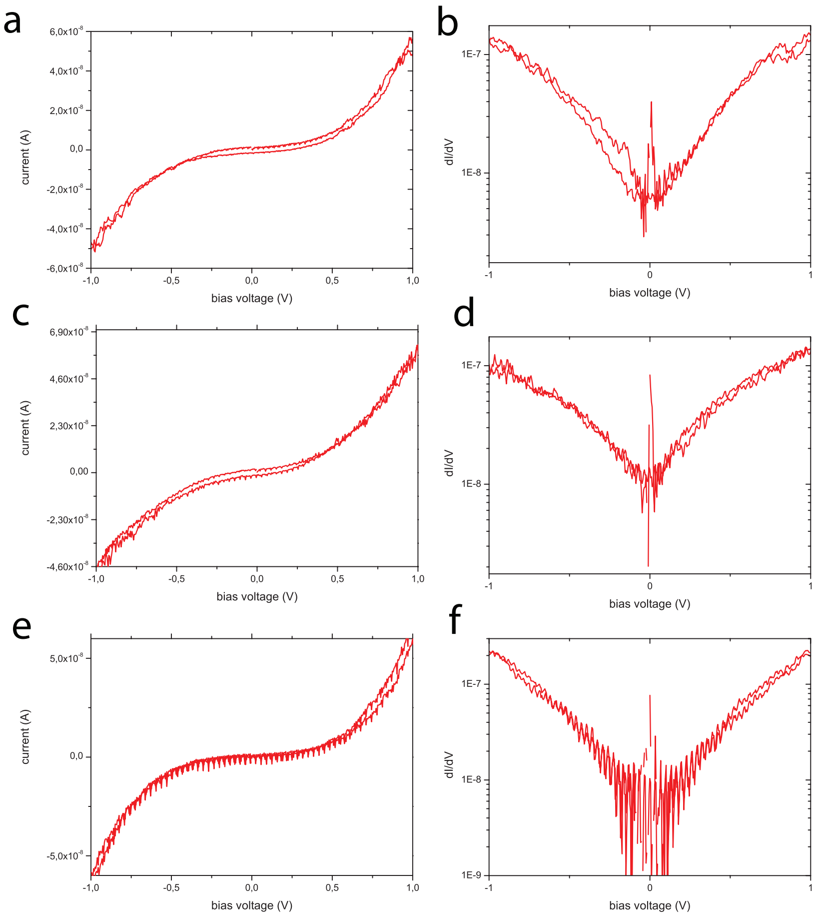

FIGURE C.10: a, c, e) typical raw I(V) traces for AQMT. b, d, f) dI/dV-traces based on the I(V)'s shown in a, c, e), respectively. The I(V)'s were first smoothed and then numerically differentiated

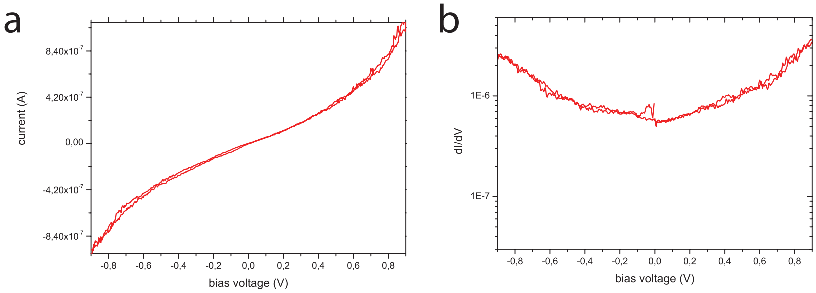

FIGURE C.11: a) typical raw I(V) trace for ACDT. b) dI/dV-trace based on the I(V) shown in a. The I(V) was first smoothed and then numerically differentiated

each I(V)-curve has first been smoothed (the blue line is almost indistinguishable from the red line). In figure C.13, we present the derivative of these two averaged I(V)-curves (again in red and blue, respectively) on a semi-log scale. For AC-DT and AQ-DT, these dI/dV's display a parabolic shape. For AQ-MT, however, the blue and red lines display negative curvature at all voltages except near $V = 0$, where an anomaly is seen. It is instructive to compare these curves to the data sets obtained by the analysis method described above. For this reason, the set of dI/dV-curves that were represented in Figs. 1c (AC-DT), 3a (AQ-DT), 3b (AQ-MT) and SC.9 (AQ-MT, "broken tip") are also plotted in Fig. SC.13a, b, c, and d respectively (in black, each curve is 99% transparent). We see that the shape of the average curves (red, blue lines) corresponds well with the individual curves, although there is some rounding off. For completeness, we note that logarithmic averaging of the absolute I(V)-curves leads to the same conclusions, i.e., a negative curvature and an anomaly is observed for AQ-MT, but not for AC-DT and AQ-DT.

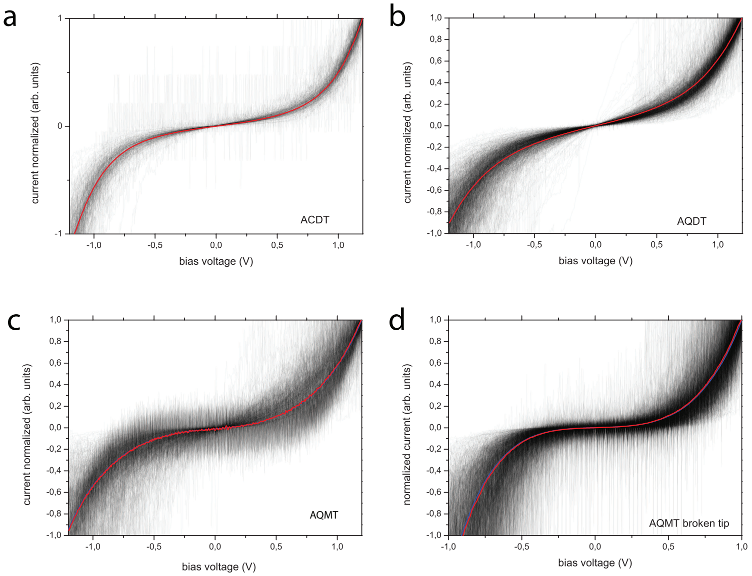

FIGURE C.12: I(V)-curves, with the current normalized. In grey, we show all the measured raw I(V)-traces. The black line represents the linearly averaged raw traces; the dark gray line represents linear average of the traces after they have been smoothed with a 50 points window. a) for ACDT, b) for AQDT, c) for AQMT and d) for AQMT with a broken tip as explained above

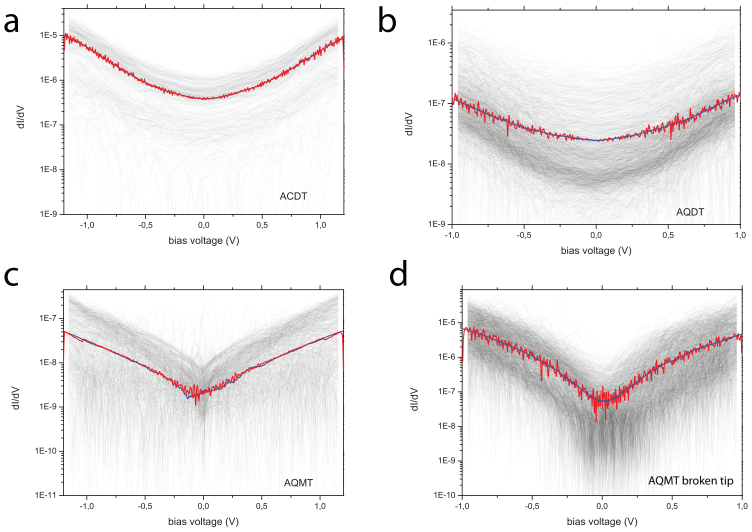

FIGURE C.13: dI/dV curves a) for ACDT, b) for AQDT, c) for AQMT and d) for AQMT with a broken tip as explained above. In grey: all the raw I(V) traces after smoothing and numerical differentiation, on a semi log scale. Black (dark gray) lines: numerical derivative of the black (dark gray) lines in the corresponding panels in Fig. C.12.

REFERENCES

[1] H. Valkenier, E. H. Huisman, P. A. van Hal, D. M. de Leeuw, R. C. Chiechi, and J. C. Hummelen, *Formation of High-Quality Self-Assembled Monolayers of Conjugated Dithiols on Gold: Base Matters*, J. Am. Chem. Soc. **133**, 4930 (2011).

[2] J. Thome, M. Himmelhaus, M. Zharnikov, and M. Grunze, *Increased Lateral Density in Alkanethiolate Films on Gold by Mercury Adsorption*, Langmuir **14**, 7435 (1998).

[3] C. D. Bain and G. M. Whitesides, *Attenuation Lengths of Photoelectrons in Hydrocarbon Films*, J. Phys. Chem. **93**, 1670 (1989).

[4] J. Enkovaara, C. Rostgaard, J. J. Mortensen, J. Chen, M. Dulak, L. Ferrighi, J. Gavnholt, C. Glinsvad, V. Haikola, H. A. Hansen, et al., *Electronic structure calculations with GPAW: a real-space implementation of the projector augmented-wave method*, J. Phys Condens. Matter **22** (2010).

[5] J. J. Mortensen, L. B. Hansen, and K. W. Jacobsen, *Real-space grid implementation of the projector augmented wave method*, Phys. Rev. B **71**, 035109 (2005).

[6] A. H. Larsen, M. Vanin, J. J. Mortensen, K. S. Thygesen, and K. W. Jacobsen, *Localized atomic basis set in the projector augmented wave method*, Phys. Rev. B **80**, 195112 (2009).

[7] J. P. Perdew, K. Burke, and M. Ernzerhof, *Generalized gradient approximation made simple*, Phys. Rev. Lett. **77**, 3865 (1996).

[8] J. M. Garcia-Lastra, C. Rostgaard, A. Rubio, and K. S. Thygesen, Phys. Rev. B **80**, 245427 (2009).

[9] D. J. Mowbray, G. Jones, and K. S. Thygesen, *Influence of functional groups on charge transport in molecular junctions*, J. Chem. Phys. **128**, 111103 (2008).

[10] S. Y. Quek, H. J. Choi, S. G. Louie, and J. B. Neaton, Nano Lett. **9**, 3949 (2009).

[11] J. Z. Chen, T. Markussen, and K. S. Thygesen, *Quantifying transition voltage spectroscopy of molecular junctions: Ab initio calculations*, Phys. Rev. B **82**, 121412 (2010).

[12] T. Markussen, J. Schiötz, and K. S. Thygesen, *Electrochemical control of quantum interference in anthraquinone-based molecular switches*, J. Chem. Phys. **132**, 224104 (2010).